5-1-2007

BVI Photometry and the Luminosity Functions of the Globular Cluster M92

Nathaniel E. Q. Paust
Space Telescope Science Institute

Brian Chaboyer
Dartmouth College

Ata Sarajedini
University of Florida

The Astronomical Journal, 133:2787–2798, 2007 June

BVI PHOTOMETRY AND THE LUMINOSITY FUNCTIONS OF THE GLOBULAR CLUSTER M92

Nathaniel E. Q. Paust
Space Telescope Science Institute, Baltimore, MD 21218, USA; npaust@stsci.edu

Brian Chaboyer
Department of Physics and Astronomy, Dartmouth College, Hanover, NH 03755, USA

and

Ata Sarajedini
Department of Astronomy, University of Florida, Gainesville, FL 32611, USA
Received 2006 April 17; accepted 2007 January 24

ABSTRACT

We present new *BVI* ground-based photometry and *VI* space-based photometry for the globular cluster M92 (NGC 6341) and examine luminosity functions in *B*, *V*, and *I* containing over 50,000 stars ranging from the tip of the red giant branch to several magnitudes below the main-sequence turnoff. Once corrected for completeness, the observed luminosity functions agree very well with theoretical models and do not show stellar excesses in any region of the luminosity function. Using reduced-χ^2 fitting, the new M92 luminosity function is shown to be an excellent match to the previously published luminosity function for M30. These points combine to establish that the "subgiant excess" found in previously published luminosity functions of Galactic globular clusters is due to deficiencies in the stellar models used at that time. Using up-to-date stellar models results in good agreement between observations and theory. Several statistical methods are presented to best determine the age of M92. These methods prove to be insensitive to the exact choice of metallicity within the published range. Using $[\mathrm{Fe/H}] = -2.17$ to match recent studies we find an age of 14.2 ± 1.2 Gyr for the cluster.

Key words: globular clusters: individual (M92) — stars: distances — stars: evolution

Online material: color figures

1. INTRODUCTION

Globular clusters are ideal locations to test stellar evolutionary models due to their single-age, single-metallicity nature. Previously, work has focused in great depth on the analysis of the color-magnitude diagrams (CMDs) of clusters, for example, in Renzini & Fusi Pecci (1988). While studies of the CMD can reveal a great deal about stellar evolution, the luminosity function (LF) of the cluster is especially powerful for determining the timescales of stellar evolution. Below the main-sequence turnoff (MSTO), the LF is primarily a reflection of the initial mass function modulated by dynamical mass segregation effects at the lowest masses. However, above the MSTO the LF reveals the progress of the hydrogen-burning shell through the star and can even give hints as to the internal structure of the star. Indeed, the enhancement in the LF known as the LF "bump" marks the hydrogen-burning shell's transition from the region previously mixed by convection into unmixed stellar material (Iben 1968).

Only with the advent of large-format CCD cameras has it become possible to obtain precise photometry of a large numbers of stars in all phases of stellar evolution. Previous studies have been largely limited to either low-precision photographic measurements or small spatial coverage and limited samples of stars. With detailed LFs, unexpected results have appeared. Bolte (1994) found an excess of stars on the subgiant branch (SGB) for the low-metallicity, $[\mathrm{Fe/H}] = -2.12$ (Harris 1996) cluster M30 (NGC 7099). The subgiant excess in M30 was further confirmed by Sandquist et al. (1999) using a higher quality data set. This SGB excess is the expected result if weakly interacting massive particle energy transport is important in stars (Faulkner & Swenson 1993). Recent LFs of the more metal-rich clusters M5 (Sandquist et al. 1996) and M3 (Rood et al. 1999) with $[\mathrm{Fe/H}] = -1.27$ and -1.57, respectively, do not show the SGB excess, suggesting that it may only be a characteristic of metal-poor clusters. However, the models used in the comparison do not include diffusion, which is a standard part of modern stellar evolution codes and the statistical basis for the SGB excess is not explicitly defined.

The LF of M92 (NGC 6341) is an ideal test for stellar modeling codes. Its metallicity, $[\mathrm{Fe/H}] = -2.27$ (Harris 1996), places it in the same abundance range as M30, which was earlier found to have a SGB excess. It is a large cluster, making it easy to measure significant numbers of stars. Its location, far from the Galactic plane ($b = 34.86°$; Harris 1996), minimizes the significance of field-star contamination. It is a fairly well studied cluster with accurately determined distance modulus and metallicity, which simplifies comparisons of the observed LF to models. Finally, previous LF studies of the cluster such as Piotto et al. (1997) and Lee et al. (2003) have not looked at the LF along the red giant branch (RGB) in order to examine the previously found excess present in M30; instead, they have concentrated on the lower MS. The Lee et al. (2003) study further supports using M92 as a test for stellar modeling codes, since examination of the mass function in that work suggests that the cluster has not been strongly affected by tidal shocks, resulting in a pure sample of cluster stars.

In the context of the above points, we herein present our analysis of a comprehensive LF study of M92 using ground-based and space-based observations. Section 2 describes these observations, while § 3 discusses the reduction of the data. Sections 4 and 5 present the CMDs and LFs. Section 6 details the stellar evolution model and discusses details in fitting the theoretical models to the observed LFs. Section 7 compares the new M92 LF to previous LFs of M92 and M30, and § 8 presents conclusions about the fits and the general state of LF modeling.

2. OBSERVATIONS

The ground-based images were collected from 2003 April 21–27 using the Hiltner 2.4 m telescope at MDM Observatory on Kitt Peak. All frames were taken using the Echelle 2048×2048 camera with a pixel scale of $0.28''$ pixel^{-1} and a total field of view of $9.56'$. To cover a significant fraction of the cluster area, short and long exposures were tiled over a $27' \times 27'$ area. For the short images, exposure times were chosen to ensure that stars at the tip of the RGB were not saturated, typically resulting in 5–15 s exposures. Two images in each filter were taken at each grid position for the short images. The exposure lengths for the longer exposures were in the range of 60–120 s depending on the filter, and three exposures were taken in each filter at each grid position. All of the images were observed under photometric conditions with average seeing of approximately $0.8''$.

The *Hubble Space Telescope* (*HST*) images were taken from the STScI archives and were collected on 2002 August 27 using the Advanced Camera for Surveys (ACS). The *HST* images were obtained with the ACS on 2002 August 27 as part of *HST* program GO-9453. The exposures cover the central $3'$ of the cluster in the F606W and F814W filters, with exposure lengths of 0.5, 5, and 90 s and 0.5, 6, and 100 s in the two filters, respectively. Because these observations were taken shortly after ACS was installed, the charge transfer efficiency corrections are negligible (Brown et al. 2005).

3. DATA REDUCTION

3.1. *Image Processing*

The ground-based images of M92 were processed using standard IRAF techniques using evening and dawn twilight flats. The archival *HST* images were processed using the STScI on-the-fly reprocessing system from the Multimission Archive at Space Telescope. The drizzled images, multiplied by the image exposure time, were used for the photometry.

3.2. *Photometry*

3.2.1. *The Ground-Based Sample*

Profile-fitting photometry was performed on the 179 image frames using the DAOPHOT and ALLSTAR programs developed by P. Stetson (Stetson 1987, 1994). In each frame, approximately 100 bright uncrowded stars were chosen to determine the point-spread function (PSF) and its variation about the frame. While the PSF stars were specifically chosen to be outside the most crowded regions of each frame, they generally did sample a large fraction of the frame and therefore map the PSF variations well. Several scripts were used to automate two passes through DAOPHOT's FIND routine and ALLSTAR to generate a photometry list for each image.

Photometry from the individual frames was filtered to remove any detection with a measured error greater than 0.1 mag. Aperture corrections were calculated using the brightest uncrowded stars on each frame. These were used to search for a spatial dependence of the aperture correction, but none was found. DAOMASTER and DAOMATCH were then used to combine the individual photometry files into one master file for each filter, requiring that a star be detected in at least two frames in each filter. These master files were filtered to contain only stars whose frame-to-frame magnitude variation was less than 0.1 mag. The *B*, *V*, and *I* master files were then matched using DAOMASTER and DAOMATCH, requiring a star to be detected in all three filters to be included in the final catalog.

3.2.2. *The HST Sample*

The space-based images were processed using the same methods as the ground-based data, although the process was simplified by the fact that there were only six images. While the same criteria for rejecting stars based on photometric errors was used, the matching criterion was relaxed to require that stars only be detected once in each filter.

3.3. *Calibration*

The instrumental magnitudes were brought onto the standard system using P. Stetson's photometric standards for M92 (Stetson 2000). Using stars brighter than 17 mag in *V*, we were able to find over 600 stars with *B*, *V*, and *I* magnitudes in common between the Stetson standards and our ground-based data. The best photometric solution to bring the data to the Stetson system was found to depend on color only to first order. The transformation equations were determined to be

$$B = b + 2.685 + 0.0537(B - V),$$

$$V = v + 1.530 - 0.0413(B - V),$$

$$I = i + 0.223 + 0.0120(V - I).$$

The residuals from the fit between the observed stars and the Stetson standards are shown in Figure 1. In all cases, the distribution of the residuals is exactly the distribution expected from the photometric errors.

The *HST* data posed an interesting problem in calibration because of the small field of view in the crowded core of the cluster. Due to confusion between stars in the core of the cluster, there were no Stetson standard stars in the field of view of the *HST* images. It was possible, however, to calibrate the *HST* photometry using our ground-based observations as secondary standards. Using the same method as in the calibration of the ground-based data, approximately 400 stars in common were compared. These stars all lie in the outer $0.5'$ of the *HST* images. In order to simplify the interpretation of the LFs, which are based on *BVI* magnitudes, the instrumental magnitudes from the *HST* data were transformed directly into *V* and *I* using the following relationships:

$$V = 606_{\rm inst} + 0.4881 + 0.0695(V - I) + 0.1510(V - I)^2,$$

$$I = 814_{\rm inst} - 0.3850 - 0.0521(V - I) + 0.0306(V - I)^2.$$

Figure 2 shows the residuals between the *HST* photometry and the ground-based photometry. The distribution matches expectations based on the photometric errors in the two data sets.

4. THE COLOR-MAGNITUDE DIAGRAMS

In total, 34,242 stars in the ground-based sample and 41,205 stars in the *HST* sample were measured. The *HST* sample is larger due to the decreased confusion in the core, which allowed a much larger number of MS stars to be detected. The *V* versus $(B - V)$ and $(V - I)$ CMDs from the terrestrial sample are shown in Figure 3. The *V* versus $(V - I)$ CMD from the *HST* sample is shown in Figure 4.

5. THE LUMINOSITY FUNCTIONS

5.1. *Completeness*

The critical task in generating a LF is determining the completeness of the photometric sample. Generally, the completeness is a function of both position relative to the cluster, due to the

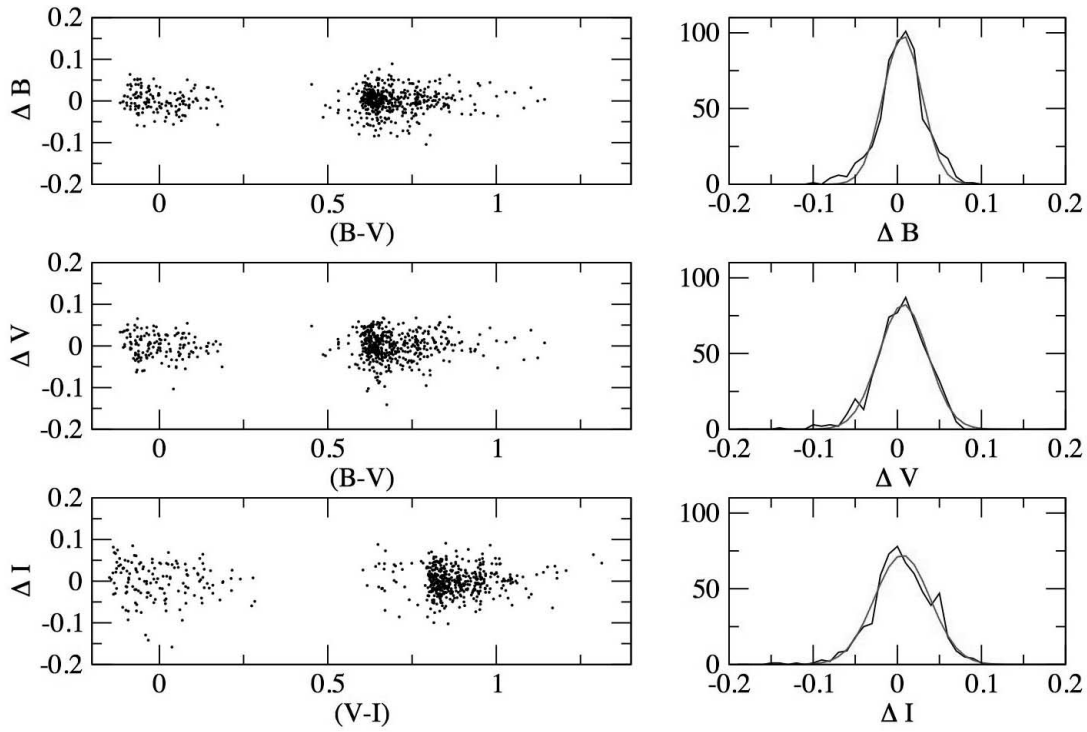

FIG. 1.—Residual distributions for the standard stars. The second column of plots shows the error distribution displayed with fitted Gaussians with standard deviations of 0.023, 0.028, and 0.033 for *B*, *V*, and *I*, respectively. These standard deviations are as expected for simple error propagation given the photometric errors. [*See the electronic edition of the Journal for a color version of this figure*.]

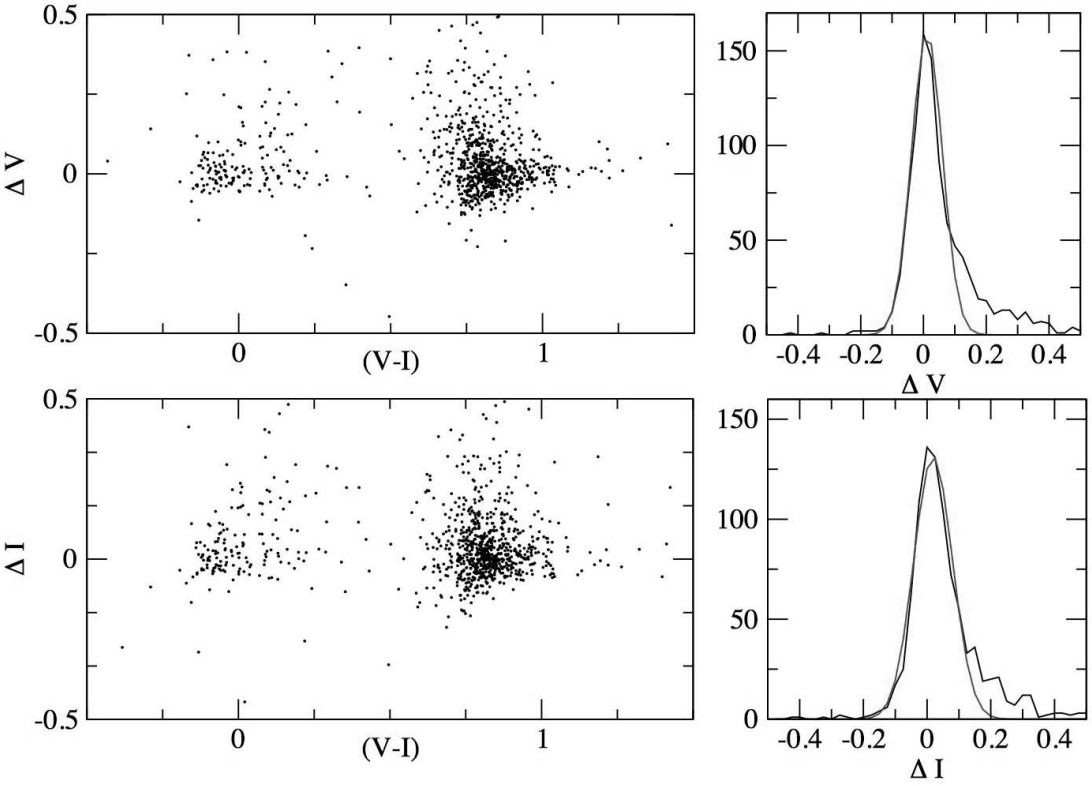

FIG. 2.—Residual distributions for the standardized *HST* sample. The residual distribution is shown overplotted with Gaussians with standard deviations of 0.05 in *V* and 0.06 in *I*. [*See the electronic edition of the Journal for a color version of this figure*.]

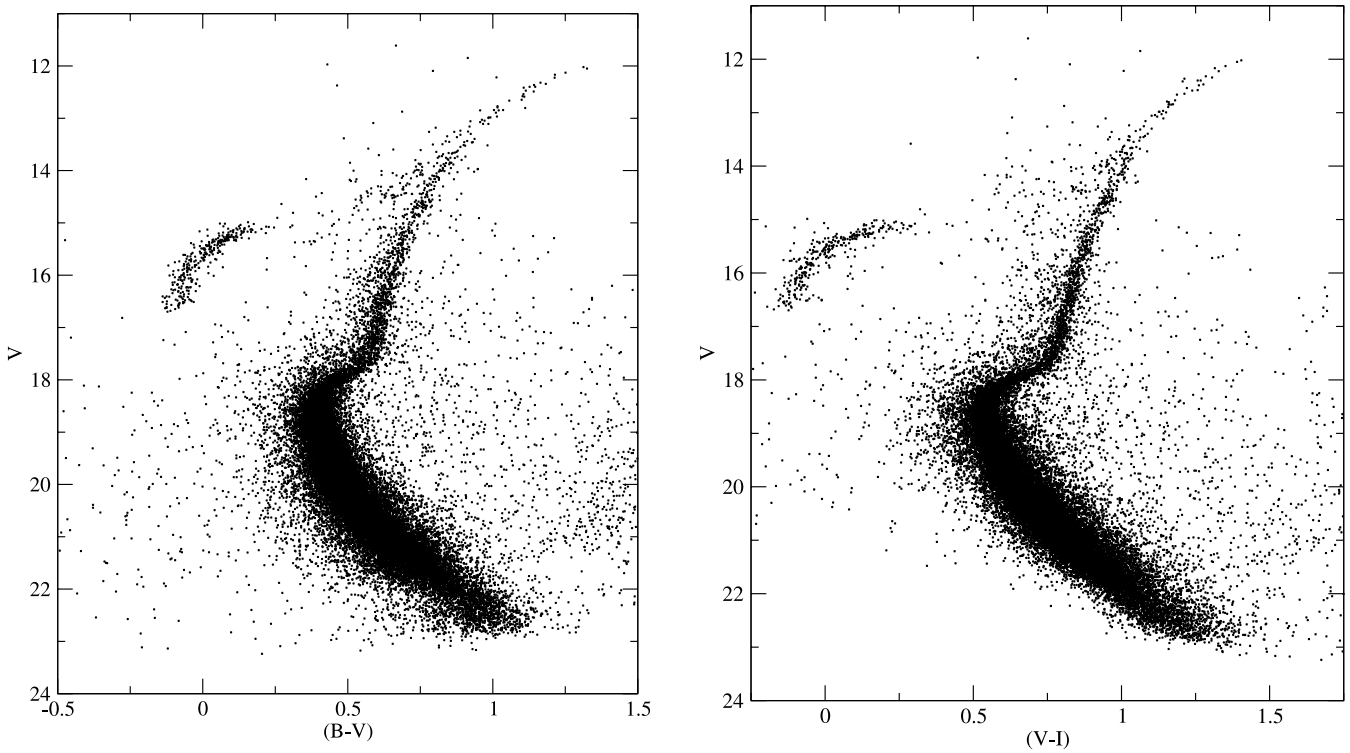

FIG. 3.—The V vs. $(B-V)$ and V vs. $(V-I)$ CMDs for the ground-based sample.

confusion in crowded regions, and magnitude. An accurate determination of the completeness is found through extensive use of artificial-star tests. These tests were performed by adding artificial stars to each image and then remeasuring photometry for the complete field to determine what fraction of the added artificial stars are recovered. Errors in the eventual LFs are governed by Poisson statistics, so large numbers of input and recovered artificial stars are needed. However, adding a large number of stars to any particular image will change the crowding and therefore the completeness. In order to balance this effect, many runs through the artificial-star routine are used with relatively small numbers of stars added in each run.

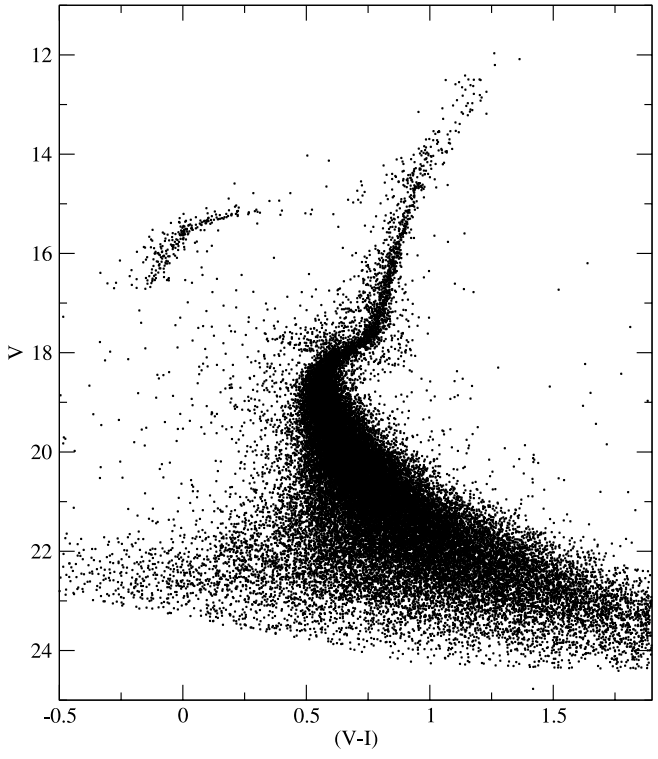

FIG. 4.—The V vs. $(V-I)$ CMD for the *HST* sample. This CMD covers an area of approximately $3' \times 3'$ and contains over 41,000 stars.

The general method used for the artificial-star tests was as follows: a master list of artificial stars with random x and y pixel positions covering the entire area imaged was created. The magnitude for the artificial stars was determined by generating random numbers covering the range of instrumental B magnitudes found during the photometry. The assigned B magnitudes were then used with the CMD ridge lines to assign V and I magnitudes to each artificial star. The result is a list of artificial stars distributed randomly across the imaged area with magnitudes and colors that match the observed cluster stars. Each star from the master list was placed at the appropriate position with the appropriate instrumental magnitude in each frame that it could have appeared. The image frames with added artificial stars were then put back through the same DAOPHOT and ALLSTAR pipeline used for the initial photometry, including the same error clipping and required number of detections during matching. In addition, the input and recovered magnitudes for the artificial stars were required to be within 0.1 mag in order to remove the possibility of real stars or blends being confused with the artificial stars. Figure 5 shows the difference between the input and recovered artificial star magnitudes as a function of V magnitude. To investigate any magnitude bias in the recovered artificial stars, the stars were divided into bins 2 mag wide, and the average difference between the input and recovered magnitude was determined. For all bins brighter than 22 mag, the bias had an absolute value of 0.002 mag or less. The final bin had a bias of 0.012. However, the last bin is beyond the completeness limit and has an order of magnitude less stars than any of the other bins. Based on this analysis, there is no

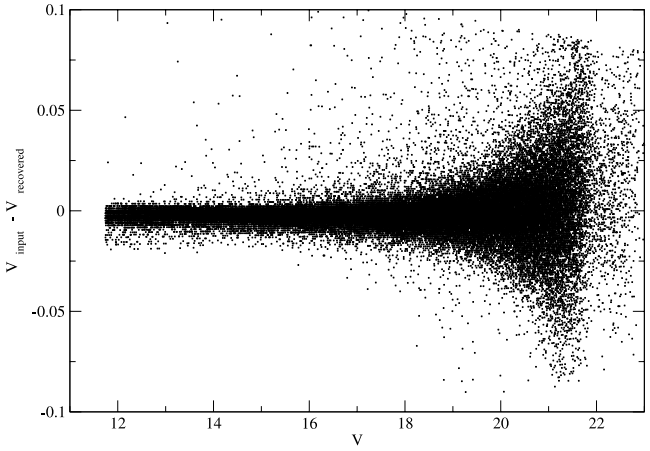

FIG. 5.—Difference between input and recovered artificial-star magnitudes for the 59,000 recovered artificial stars as a function of *V*. The average bias is insignificant at −0.0005 mag in *V* and similar amounts in *B* and *I*.

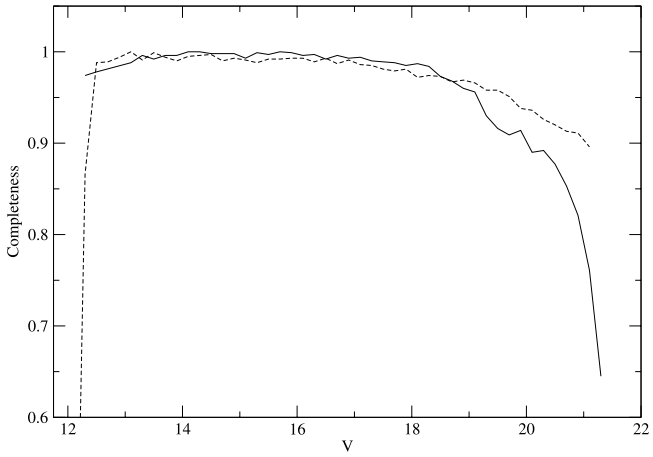

FIG. 6.—Completeness of the ground-based (*solid line*) and space-based (*dashed line*) data as a function of *V* magnitude. The completeness limits quoted for the LFs are slightly different than might be expected from these lines, since they are based on completeness as sampled by the positions of the cluster stars rather the random positions of the artificial stars.

significant bias in the artificial-star magnitudes. In all, 24 sets of artificial stars, taking approximately 36 CPU hours per set, were added to the images for a total of over 91,000 input stars and 59,000 recovered stars.

Due to the relatively small number of images in the space-based data, it was possible to use a larger number of artificial-star runs in a reasonable amount of time. Using the same procedure, over 267,000 artificial stars were added, and over 203,000 were recovered from the images after processing 90 sets of artificial stars. The completeness of the data sets as a function of magnitude is shown in Figure 6. The lower completeness at the bright end is due to bright stars saturating in some of the images.

5.2. *Computing the Luminosity Function*

There are two main steps in transforming the photometric data into the LF. First, field stars, horizontal branch (HB) stars, and asymptotic giant branch (AGB) stars must be removed to produce a pure sample of stars on the MS and RGB. The field stars, HB stars, and AGB stars were removed by clipping all stars more than 3 σ in color from the fiducial reference line. To find the fiducial line, a box was run across the CMD in color at different magnitudes. The set of points in color that maximizes the population in the box as a function of magnitude defines the fiducial line. This method will not remove any field stars that lie along the MS and RGB, but the density of field stars is low enough that the resulting LF is not significantly affected. This is confirmed by the Besancon stellar population synthesis models (Robin et al. 2003), which predict approximately 10 field stars along the upper half of the RGB. The photometric clipping method is ambiguous at the top of the RGB, where the AGB and RGB nearly merge. In this region, extraneous AGB stars were removed manually.

Completeness corrections were accomplished by weighting each star individually. A grid of completeness as a function of radius from the cluster center and magnitude was constructed and then used to assign a weight of completeness $(m, r)^{-1}$ to each star. The LF was then constructed by summing the weights of stars in each magnitude bin. The completeness limit was defined as the magnitude at which the average weight per star in the bin was equal to 2, roughly the point where the data is 50% complete. The completeness in the *V* band as a function of magnitude is shown in Figure 6. The error bars on the LF are Poisson errors given by

$$\sigma(N_i) = N_i\sqrt{1/n_i + 1/a_i + 1/b_i},$$

where N_i is the summed weights of stars in the magnitude bin, n_i is the number of stars in the magnitude bin, a_i is the number of recovered artificial stars in the magnitude bin, and b_i is the number of input artificial stars in the magnitude bin. The number of stars in each bin is the dominant source of uncertainty rather than the number of input or recovered artificial stars.

This weighting method revealed one shortcoming of the ground-based data, namely, the fact that, due to the high stellar density, no stars fainter than the SGB were detected in the central 2′ of the cluster. This introduces a skew into the LF, since the area being sampled at each magnitude is different. This could be corrected by defining a cluster profile based on brighter, more complete stars and then correcting the numbers of fainter, less complete stars. This method has been used in previous papers in the literature. However, any correction would assume that the cluster has the same profile for high- and low-mass stars and would completely disregard any mass segregation in the cluster, as was found for M3 by Rood et al. (1999). This method could also cause problems, since errors in the numbers of bright stars, with poor error statistics, would be propagated through the entire LF. Also, because the size of the central hole depends very strongly on magnitude, extreme care would be required to avoid artificially generating an excess or deficiency at points in the LF. To simplify the analysis of the LF, the central area of the ground-based data, containing approximately 11,000 stars, was removed. The resulting completeness limits are $B = 22.1$, $V = 21.3$, and $I = 20.5$. The *V* LFs from the ground, *HST*, and combined data sets are shown in Figure 7 and are representative of the LFs in the other bands. The ground-based LFs are listed in Table 1.

The *HST* sample displayed reasonable completeness across the entire field, unlike the ground-based sample, so the entire catalog was used to create the LFs using the procedure outlined above. Due to the relatively small field of view of the ACS, very few stars near the tip of the RGB were detected, resulting in a very noisy LF. The completeness limits are $V = 21.1$ and $I = 20.1$, limited largely by the short exposure times. The LFs from the *HST* sample are listed in Table 2.

Combining the *HST* data from the cluster's central region with the ground-based photometry of the outer region, it was possible to create a composite LF covering a full 27′ square area of the cluster. The composite LF contains data for over 54,400 weighted stars. The combined LFs are listed in Table 3. The completeness

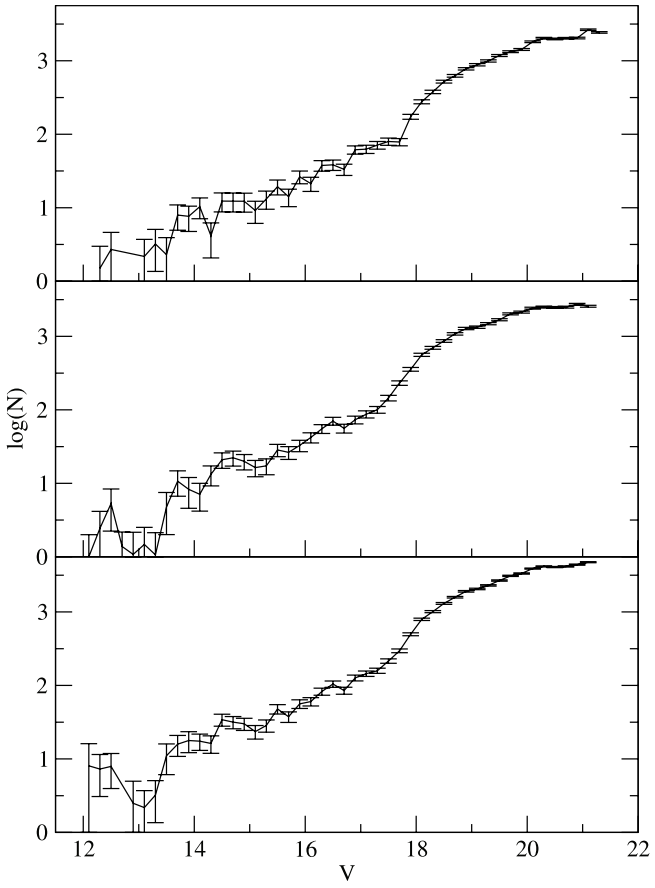

FIG. 7.—*Top to bottom*: Ground-based *V* LF, *HST V* LF, and combined *V* LF. In all three LFs, the error bars are the 1 σ Poisson errors. The LFs in *B* and *I* look very similar and are of equal quality.

limits for this sample are taken to be the completeness limits of the *HST* sample.

6. THEORETICAL LF MODELS AND FITTING

To produce the theoretical LFs for comparison to the observed data, stellar models were created using the Dartmouth Stellar Evolution Code (DSEP; Chaboyer et al. 2001). These models used the VandenBerg & Clem (2003) color transformations. A catalog of theoretical LFs was created with ages stepped by 0.1 Gyr from 11.6 to 16.5 Gyr. The models use scaled solar compositions, while globular clusters are typically enhanced in their α-element (O, Mg, Si, S, and Ca) abundances. As noted by Chieffi et al. (1991) and Chaboyer et al. (1992), scaled solar composition models are nearly identical to α-element enhanced models, provided one modifies the relationship between [Fe/H] and the heavy-element mass fraction *Z*. The modification assumed $[\alpha/\mathrm{Fe}] = +0.40$. Metallicities of $[\mathrm{Fe/H}] = -2.11, -2.14, -2.17, -2.20, -2.23, -2.27$, and -2.31 were chosen to sample the published range of $-2.24 \pm .08$ (Zinn & West 1984), -2.27 (Harris 1996), and -2.38 ± 0.07 (Kraft & Ivans 2003). The majority of the comparisons between the observed and theoretical LFs were completed using the $[\mathrm{Fe/H}] = -2.17$ models, since they are the closest metallicity match to the recent Kraft & Ivans (2003) measurements after being modified for the scaled solar assumption. All of the statistical tests proved to be insensitive to metallicity in the studied range.

One of main parameters in fitting the theoretical LFs to the observed ones is the distance modulus. To ensure that this represents the absolute distance modulus, the observed LFs must be corrected for extinction. A standard extinction-color excess relation was used, $A(V) = 3.1E(B - V)$, with the published value of the color excess being 0.02 for M92 (Harris 1996). Extinction in the *I* band was calculated assuming $E(V - I) = 1.25E(B - V)$ (Dean et al. 1978). All extinctions were computed on the *B*,*V*, and *I* magnitudes. Sirianni et al. (2005) suggest that reddening and extinction should be considered in the native 606W and 814W filters for the space-based observations due to the slight differences with the standard *V* and *I* filters. Due to the low reddening to M92, the difference in methodology corresponds to a difference of 0.008 mag in the *V* filter and 0.001 mag in the *I* filter.

Three separate statistical methods were used to determine the best match between the observed and theoretical LFs. First, a reduced-χ^2-fitting method based on Bevington & Robinson (1992) was used to find the best match between the theoretical and observed LFs in all three filters simultaneously. During the reduced-χ^2 minimization, the absolute distance modulus was allowed to vary, while the normalization was set by the total number of stars brighter than the completeness limit in the LF. Regardless of the theoretical model used, the reduced-χ^2 values were similar, with values around 0.9 with a wide range of distance moduli (± 0.3 mag) and ages (± 1.2 Gyr) producing seemingly reasonable fits. The reduced-χ^2 fits covered a range from the tip of the RGB to 1 mag below the MSTO, to $V = 18.9$. This covers a mass range from 0.73 to 0.77 $M_\odot$ and therefore tests the relative numbers of stars on the RGB and MS rather than being sensitive to the cluster IMF. Standard probability tables for the reduced-χ^2 statistic assume Gaussian errors, while the errors in the LF come from Poisson counting. As a result, we employ a Monte Carlo simulation to estimate the statistical significance of our LF comparisons. In the simulation, 10^6 realizations of the M92 LF were generated using the quoted errors. The reduced-χ^2 values between the original LF and the realizations were then computed to generate a probability table. Reduced-χ^2 values of 0.9 or less are found 75% of the time, showing a good match between the observed LF and the theoretical LFs. A typical best match between the theoretical and observed ground-based LFs is shown in Figure 8.

6.1. *The K-S Test*

In order to get a better constraint on the data, the observed and theoretical data were compared using the Kolmogorov-Smirnov (K-S) test. The K-S test maps the maximum difference between the theoretical cumulative LF and the observed cumulative LF and is therefore somewhat immune to the potential blending of stars between bins by photometric errors in the conventional LF.

To complete the K-S test, a subsection of the LFs from approximately 0.5 mag fainter than the tip down to the MSTO was defined. The cumulative LF from this region is then compared to the cumulative theoretical LF while stepping through the absolute distance modulus. Ages from 11.6 to 16.5 Gyr were examined in 100 Myr increments. The K-S probability statistic was then used to find the best match. The error in age and absolute distance modulus was assumed to be given by the error ellipse traced by the 50% contour line. There was no significant difference between the different metallicity models, so comparisons have been made using the model closest to the Kraft & Ivans (2003) metallicity, the $[\mathrm{Fe/H}] = -2.17$ model. This results in good agreement between the observed LFs and the model, giving an age of 14.2 ± 1.2 Gyr. This result is shown in Figure 9.

7. COMPARISONS

7.1. *Previous M92 Luminosity Functions*

Lee et al. (2003) published an LF for stars fainter than the MSTO, which serves as a good check for the LF presented in this

TABLE 1
THE GROUND-BASED LUMINOSITY FUNCTIONS

Magnitude	N_B	σ_B	Comp_B	$\log(N_B)$	N_V	σ_V	Comp_V	$\log(N_V)$	N_I	σ_I	Comp_I	$\log(N_I)$
10.9	...	...	...	...	...	...	...	...	1.50	1.50	0.67	0.18
11.3	...	...	...	...	...	...	...	...	2.71	1.93	0.74	0.43
11.9	...	...	...	...	...	...	...	...	2.17	1.54	0.92	0.34
12.1	...	...	...	...	...	...	...	...	1.18	1.18	0.85	0.07
12.3	...	...	...	...	1.50	1.50	0.67	0.18	3.05	1.77	0.98	0.48
12.5	...	...	...	...	2.71	1.92	0.74	0.43	2.35	1.67	0.85	0.37
12.7	...	...	...	...	...	...	...	...	5.58	2.52	0.90	0.75
12.9	...	...	...	...	...	...	...	...	6.55	2.70	0.92	0.82
13.1	...	...	...	...	2.17	1.54	0.92	0.34	13.76	3.90	0.95	1.14
13.3	...	...	...	...	3.22	1.86	0.93	0.51	2.08	1.48	0.96	0.32
13.5	1.50	1.50	0.67	0.18	2.29	1.62	0.87	0.36	9.28	3.13	0.97	0.97
13.7	2.71	1.92	0.74	0.43	7.94	3.00	0.88	0.90	12.21	3.58	0.98	1.09
13.9	...	...	...	...	7.64	2.89	0.92	0.88	12.27	3.60	0.98	1.09
14.1	2.17	1.54	0.92	0.34	10.34	3.27	0.97	1.02	5.14	2.31	0.97	0.71
14.3	5.51	2.48	0.91	0.74	4.15	2.08	0.96	0.62	10.24	3.28	0.98	1.01
14.5	3.30	1.91	0.91	0.52	12.33	3.56	0.97	1.09	16.25	4.15	0.99	1.21
14.7	10.19	3.43	0.88	1.01	12.29	3.55	0.98	1.09	15.27	4.01	0.98	1.18
14.9	12.44	3.64	0.97	1.10	12.25	3.54	0.98	1.09	13.13	3.70	0.99	1.12
15.1	6.21	2.55	0.97	0.79	9.18	3.06	0.98	0.96	28.36	5.53	0.99	1.45
15.3	11.32	3.45	0.97	1.05	13.20	3.66	0.99	1.12	24.38	5.11	0.98	1.39
15.5	14.29	3.87	0.98	1.16	19.36	4.44	0.98	1.29	37.49	6.39	0.99	1.57
15.7	10.20	3.26	0.98	1.01	14.13	3.78	0.99	1.15	31.32	5.81	0.99	1.50
15.9	14.26	3.86	0.98	1.15	26.35	5.17	0.99	1.42	34.28	6.07	0.99	1.54
16.1	17.34	4.27	0.98	1.24	21.30	4.65	0.99	1.33	60.50	8.25	0.99	1.78
16.3	18.23	4.36	0.99	1.26	37.55	6.17	0.99	1.58	57.51	8.07	0.97	1.76
16.5	18.16	4.35	0.99	1.26	38.38	6.23	0.99	1.58	67.29	8.76	0.98	1.83
16.7	26.45	5.30	0.98	1.42	33.26	5.79	0.99	1.52	82.66	9.80	0.98	1.92
16.9	37.52	6.36	0.99	1.57	61.50	7.88	0.99	1.79	54.99	7.82	0.98	1.74
17.1	37.40	6.33	0.99	1.57	62.69	8.03	0.97	1.80	90.68	10.27	0.98	1.96
17.3	37.32	6.32	0.99	1.57	71.24	8.51	0.98	1.85	137.97	13.08	0.97	2.14
17.5	64.54	8.45	0.99	1.81	79.70	9.02	0.98	1.90	214.99	17.26	0.94	2.33
17.7	64.67	8.54	0.97	1.81	78.44	8.94	0.98	1.90	317.48	21.87	0.93	2.50
17.9	77.49	9.38	0.98	1.89	173.31	13.29	0.98	2.24	459.35	27.87	0.94	2.66
18.1	84.71	9.85	0.98	1.93	277.04	17.22	0.94	2.44	619.16	33.68	0.95	2.79
18.3	154.92	13.87	0.98	2.19	377.53	20.07	0.94	2.58	776.17	39.77	0.94	2.89
18.5	323.17	22.10	0.95	2.51	519.89	23.53	0.94	2.72	956.42	46.45	0.86	2.98
18.7	402.21	25.40	0.94	2.60	624.60	25.63	0.95	2.80	1038.20	49.25	0.87	3.02
18.9	511.42	29.99	0.94	2.71	777.38	28.71	0.94	2.89	1331.19	59.16	0.86	3.12
19.1	641.40	34.89	0.95	2.81	883.56	32.18	0.85	2.95	1501.23	64.31	0.87	3.18
19.3	733.42	38.38	0.94	2.87	993.66	33.96	0.86	3.00	1754.11	72.07	0.84	3.24
19.5	835.87	42.97	0.86	2.92	1179.65	37.06	0.86	3.07	2263.92	88.63	0.75	3.36
19.7	893.22	45.04	0.86	2.95	1329.35	39.27	0.86	3.12	2366.36	89.34	0.76	3.37
19.9	1070.88	52.23	0.86	3.03	1424.55	40.10	0.89	3.15	2551.47	93.03	0.77	3.41
20.1	1162.87	55.35	0.87	3.07	1813.34	49.21	0.75	3.26	2754.03	99.54	0.73	3.44
20.3	1268.80	58.27	0.88	3.10	2029.10	51.77	0.76	3.31	3147.71	111.43	0.64	3.50
20.5	1500.95	67.81	0.80	3.18	1982.14	51.20	0.76	3.30	2631.77	98.29	0.68	3.42
20.7	1654.86	74.35	0.75	3.22	2025.72	50.90	0.78	3.31	...	...	...	...
20.9	1766.34	76.57	0.76	3.25	2036.92	50.45	0.80	3.31	...	...	...	...
21.1	1732.39	75.63	0.76	3.24	2645.26	65.72	0.61	3.42	...	...	...	...
21.3	1757.00	75.71	0.78	3.25	2432.63	61.47	0.64	3.39	...	...	...	...
21.5	1713.49	74.52	0.80	3.23	...	...	...	...	...	...	...	...
21.7	2111.74	91.10	0.65	3.33	...	...	...	...	...	...	...	...
21.9	2116.93	93.42	0.62	3.33	...	...	...	...	...	...	...	...
22.1	1871.44	86.28	0.66	3.27	...	...	...	...	...	...	...	...

paper on the low-mass end. The shape of the Lee et al. LF agrees very well with our LF over the range $V = 18.5 - 20.9$, giving a reduced-χ^2 value of 0.52 once the two LFs are normalized. The match between the LFs is shown in Figure 10.

7.2. *The M30 Luminosity Function*

Previous work such as Sandquist et al. (1999) has shown that the LF of M30 has an excess of stars on the SGB when compared with stellar models. It is not clear whether this behavior is particular to M30 or is a general characteristic of low-metallicity globular clusters. To compare the LFs from M30 and M92, the reduced χ^2 between the two cluster LFs, ignoring the small metallicity difference, was calculated. To find the minimum reduced χ^2, the distance modulus and normalization of M30 were allowed to vary. Assuming a distance modulus of 14.64 for M92, the best fits were found using a distance modulus of 14.92 for the

TABLE 2

THE *HST* LUMINOSITY FUNCTIONS

Magnitude	N_V	σ_V	Comp_V	$\log(N_V)$	N_I	σ_I	Comp_I	$\log(N_I)$
10.7.....	...	...	...	...	1.00	1.00	1.00	0.00
10.9.....	...	...	...	...	2.43	1.72	0.82	0.39
11.1.....	...	...	...	...	1.97	1.97	0.51	0.29
11.3.....	...	...	...	...	4.72	2.73	0.64	0.67
11.5.....	...	...	...	...	...	...	...	...
11.7.....	...	...	...	...	1.08	0.76	1.86	0.03
11.9.....	...	...	...	...	2.54	1.47	1.18	0.40
12.1.....	1.00	1.00	1.00	0.00	...	...	...	...
12.3.....	2.43	1.72	0.82	0.39	3.13	2.22	0.64	0.50
12.5.....	5.31	3.07	0.57	0.73	9.28	3.80	0.65	0.97
12.7.....	1.38	0.80	2.17	0.14	3.07	2.17	0.65	0.49
12.9.....	1.08	1.08	0.93	0.03	8.42	3.77	0.59	0.93
13.1.....	1.48	1.04	1.36	0.17	7.21	2.95	0.83	0.86
13.3.....	1.06	1.06	0.94	0.03	9.22	3.27	0.87	0.96
13.5.....	4.75	2.75	0.63	0.68	16.22	4.36	0.86	1.21
13.7.....	10.73	4.06	0.65	1.03	25.19	5.55	0.83	1.40
13.9.....	8.28	3.71	0.60	0.92	16.25	4.37	0.86	1.21
14.1.....	7.09	2.90	0.85	0.85	13.37	3.73	0.97	1.13
14.3.....	13.24	4.01	0.83	1.12	17.38	4.24	0.98	1.24
14.5.....	20.96	4.97	0.86	1.32	24.40	5.03	0.98	1.39
14.7.....	22.27	5.14	0.85	1.35	20.32	4.58	0.98	1.31
14.9.....	19.91	4.72	0.90	1.30	26.29	5.20	0.99	1.42
15.1.....	16.39	4.12	0.98	1.21	32.82	5.87	0.98	1.52
15.3.....	17.30	4.22	0.98	1.24	41.03	6.58	0.98	1.61
15.5.....	28.47	5.43	0.98	1.45	55.22	7.66	0.98	1.74
15.7.....	26.36	5.21	0.99	1.42	60.17	7.99	0.98	1.78
15.9.....	32.73	5.84	0.98	1.51	55.84	7.67	0.99	1.75
16.1.....	42.05	6.65	0.98	1.62	68.16	8.56	0.97	1.83
16.3.....	55.24	7.64	0.98	1.74	87.98	9.79	0.97	1.94
16.5.....	70.36	8.64	0.98	1.85	91.69	9.98	0.97	1.96
16.7.....	56.03	7.67	0.98	1.75	108.80	10.83	0.98	2.04
16.9.....	73.24	8.86	0.97	1.86	137.57	12.27	0.98	2.14
17.1.....	87.13	9.73	0.96	1.94	205.70	15.45	0.95	2.31
17.3.....	100.43	10.40	0.98	2.00	270.88	18.11	0.94	2.43
17.5.....	144.85	12.59	0.98	2.16	410.81	22.74	0.96	2.61
17.7.....	231.52	16.38	0.96	2.36	537.74	26.64	0.96	2.73
17.9.....	355.63	21.01	0.95	2.55	757.05	32.76	0.96	2.88
18.1.....	561.05	27.33	0.95	2.75	997.94	39.43	0.93	3.00
18.3.....	697.94	31.22	0.96	2.84	1276.49	46.31	0.93	3.11
18.5.....	864.78	35.83	0.95	2.94	1401.20	48.64	0.94	3.15
18.7.....	1080.69	41.78	0.93	3.03	1561.22	52.28	0.94	3.19
18.9.....	1279.05	46.23	0.93	3.11	1806.69	57.45	0.94	3.26
19.1.....	1332.30	47.48	0.93	3.12	2182.04	66.22	0.88	3.34
19.3.....	1486.76	51.28	0.94	3.17	2444.68	71.29	0.89	3.39
19.5.....	1683.37	55.83	0.92	3.23	2823.79	78.90	0.89	3.45
19.7.....	2021.90	64.00	0.89	3.31	2941.16	80.48	0.89	3.47
19.9.....	2137.29	66.42	0.88	3.33	3020.60	81.24	0.91	3.48
20.1.....	2419.77	72.77	0.89	3.38	3399.52	90.58	0.81	3.53
20.3.....	2502.94	74.27	0.89	3.40	3081.61	83.45	0.84	3.49
20.5.....	2475.90	73.40	0.90	3.39	2933.70	79.82	0.84	3.47
20.7.....	2496.91	74.58	0.87	3.40	2395.66	68.53	0.86	3.38
20.9.....	2730.19	80.55	0.82	3.44	2121.00	62.69	0.86	3.33
21.1.....	2572.96	77.24	0.83	3.41	2191.36	66.77	0.77	3.34

TABLE 3

THE COMBINED LUMINOSITY FUNCTIONS

Magnitude	N_V	σ_V	Comp_V	$\log(N_V)$	N_I	σ_I	Comp_I	$\log(N_I)$
10.9.....	...	...	...	...	1.50	1.50	0.67	0.18
11.1.....	...	...	...	...	9.51	5.49	0.32	0.98
11.3.....	...	...	...	...	12.23	6.12	0.33	1.09
11.5.....	...	...	...	...	...	...	...	...
11.7.....	...	...	...	...	2.49	2.49	0.40	0.40
11.9.....	...	...	...	...	2.17	1.54	0.92	0.34
12.1.....	8.05	8.05	0.12	0.91	1.18	1.18	0.85	0.07
12.3.....	7.28	4.21	0.41	0.86	10.19	4.56	0.49	1.01
12.5.....	7.91	3.96	0.51	0.90	11.86	4.84	0.51	1.07
12.7.....	...	...	...	...	5.58	2.50	0.90	0.75
12.9.....	2.49	2.49	0.40	0.40	16.84	5.61	0.53	1.23
13.1.....	2.17	1.54	0.92	0.34	20.97	4.81	0.91	1.32
13.3.....	3.22	1.86	0.93	0.51	10.18	3.39	0.88	1.01
13.5.....	11.05	4.94	0.45	1.04	25.50	5.32	0.90	1.41
13.7.....	15.83	5.01	0.63	1.20	35.45	6.58	0.82	1.55
13.9.....	17.79	5.63	0.56	1.25	27.41	5.48	0.91	1.44
14.1.....	17.43	4.36	0.92	1.24	16.49	4.12	0.97	1.22
14.3.....	16.27	4.35	0.86	1.21	26.62	5.22	0.98	1.43
14.5.....	34.18	6.35	0.85	1.53	38.66	6.27	0.98	1.59
14.7.....	31.71	5.99	0.88	1.50	35.58	6.01	0.98	1.55
14.9.....	30.05	5.68	0.93	1.48	34.38	5.90	0.99	1.54
15.1.....	23.55	4.91	0.98	1.37	59.16	7.77	0.98	1.77
15.3.....	28.51	5.39	0.98	1.45	61.34	7.92	0.98	1.79
15.5.....	47.83	6.98	0.98	1.68	85.56	9.34	0.98	1.93
15.7.....	37.47	6.16	0.99	1.57	86.16	9.40	0.98	1.94
15.9.....	56.06	7.56	0.98	1.75	88.11	9.45	0.99	1.95
16.1.....	60.31	7.85	0.98	1.78	119.41	11.04	0.98	2.08
16.3.....	82.59	9.18	0.98	1.92	137.33	11.91	0.97	2.14
16.5.....	104.43	10.34	0.98	2.02	148.79	12.36	0.98	2.17
16.7.....	85.20	9.30	0.99	1.93	181.88	13.67	0.97	2.26
16.9.....	126.53	11.36	0.98	2.10	186.55	13.79	0.98	2.27
17.1.....	144.65	12.23	0.97	2.16	278.08	17.02	0.96	2.44
17.3.....	158.51	12.73	0.98	2.20	389.58	20.25	0.95	2.59
17.5.....	215.00	14.87	0.97	2.33	597.74	25.10	0.95	2.78
17.7.....	295.86	17.49	0.97	2.47	798.94	29.13	0.94	2.90
17.9.....	497.36	22.82	0.96	2.70	1154.05	34.91	0.95	3.06
18.1.....	793.09	28.96	0.95	2.90	1506.07	40.25	0.93	3.18
18.3.....	1009.64	32.71	0.94	3.00	1907.65	45.36	0.93	3.28
18.5.....	1305.95	37.33	0.94	3.12	2190.85	49.24	0.90	3.34
18.7.....	1585.66	41.33	0.93	3.20	2428.96	51.88	0.90	3.39
18.9.....	1908.09	45.23	0.93	3.28	2916.14	56.89	0.90	3.46
19.1.....	2057.72	47.83	0.90	3.31	3410.82	62.72	0.87	3.53
19.3.....	2295.62	50.40	0.90	3.36	3909.42	67.44	0.86	3.59
19.5.....	2671.86	54.73	0.89	3.43	4688.35	75.42	0.82	3.67
19.7.....	3100.09	59.62	0.87	3.49	4890.62	76.79	0.83	3.69
19.9.....	3331.05	61.73	0.87	3.52	5108.86	77.97	0.84	3.71
20.1.....	3887.75	68.44	0.83	3.59	5669.78	85.82	0.77	3.75
20.3.....	4169.43	70.99	0.83	3.62	5718.65	88.78	0.73	3.76
20.5.....	4081.43	69.98	0.83	3.61	...	...	...	...
20.7.....	4158.33	70.97	0.83	3.62	...	...	...	...
20.9.....	4402.63	74.05	0.80	3.64	...	...	...	...
21.1.....	4744.25	81.59	0.71	3.68	...	...	...	...

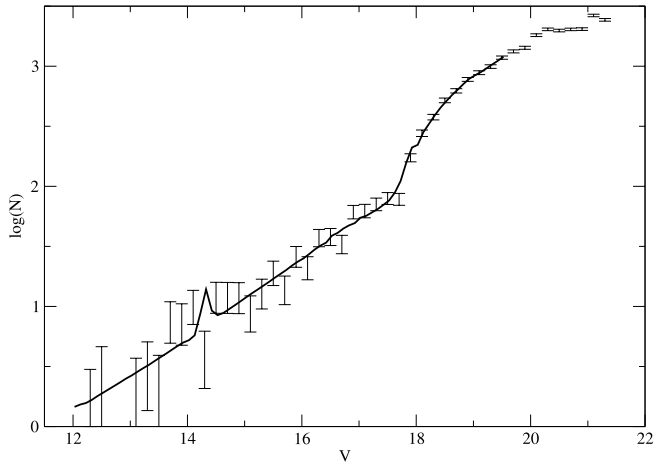

FIG. 8.—Theoretical 13.9 Gyr [Fe/H] = −2.17 LF (*solid line*) plotted with the observed *V* LF from the ground-based sample (*error bars*). The reduced χ^2 is 0.96. The *B* and *I* fits have equal quality.

V LF and a distance modulus of 14.82 for the *I* LF. This matches well with the distance modulus of 14.87 ± 0.12 found by Sandquist et al. (1999), assuming a reddening of $E(V-I) = 0.06$. The resulting reduced-χ^2 values are 0.26 in *V* and 0.36 in *I* and suggest that the LFs for M30 and M92 are very similar. Given the excellent agreement between the theoretical LFs and the M92 LFs and given the extreme similarity between the M92 LFs and previous M30 LFs, there seems to be no problem with current stellar evolution models, in contrast to previous results of Sandquist et al. (1999). The match between the M30 and M92 *V* LFs is shown in Figure 11 and is also representative of the quality of the fit in the *I* band.

In addition, the Sandquist et al. (1999) LF was directly compared to models with [Fe/H] = −2.02 and −2.42 to bracket the nominal metallicity. Allowing for a slight uncertainty in the distance modulus and normalizing the theoretical LFs to match the observed LFs, reduced-χ^2 values of 1.16 and 0.95 were found for the two models. Using the generated probability table based on Poisson errors, we find that a reduced-χ^2 value less than 0.95 is found 53% of the time, and a value of 1.16 is found 25% of the time. From this, we can conclude that the M30 LFs of Sandquist et al. (1999) are well fitted by DSEP models.

Adding further support to this argument is a direct comparison of the LFs used in Sandquist et al. (1999) to current DSEP LFs. Figure 12 compares the standard DSEP model, including diffusion and the most recent reaction rate for $^{14}N + P \rightarrow {}^{15}O + \gamma$, the slowest rate in the CNO cycle, from Formicola et al. (2004) to models with the old and new rates without diffusion and VandenBerg et al. (2006) models. All of the LFs are at the same metallicity and are 14 Gyr old. The Sandquist et al. (1999) paper used earlier

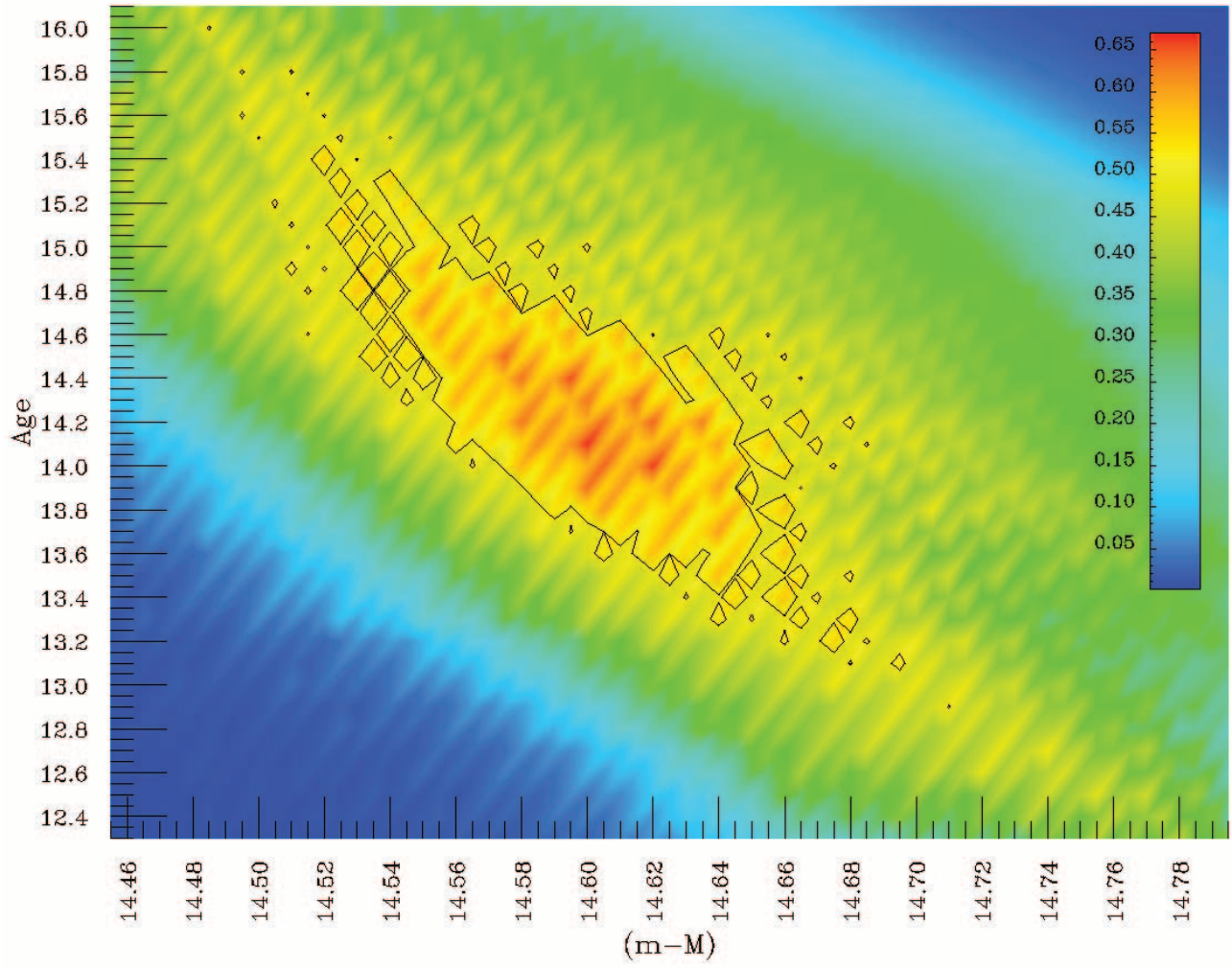

FIG. 9.—K-S test results for [Fe/H] = −2.17 models. The color scale gives the confidence as a percentage from the K-S test; the contours are drawn at the 50% level.

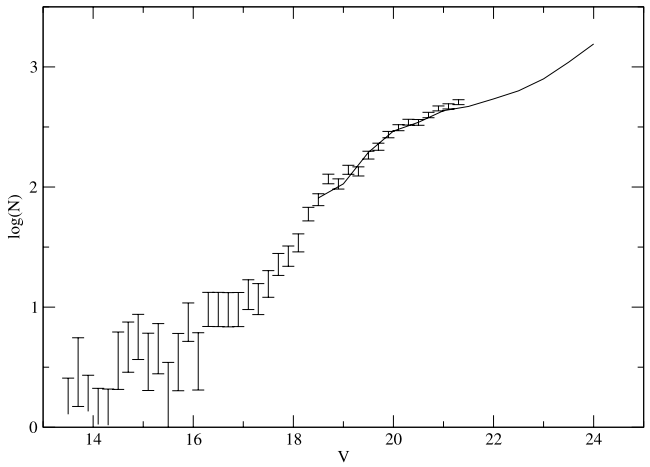

FIG. 10.—Lee et al. (2003) LF and our LF in the V band. Our LF has 1 σ error bars, while the Lee et al. LF is plotted without error bars for clarity.

versions of the VandenBerg et al. (2006) models. From the figure, it is apparent that the VandenBerg et al. (2006) models are similar to the DSEP no-diffusion models. Compared to the standard DSEP model, the VandenBerg et al. (2006) models have 9% fewer stars along the RGB. The difference explains the deviation found between the observed LF and the theoretical LFs in Sandquist et al. (1999).

This underscores a point raised in Gallart et al. (2005), that a variety of different model libraries should be used before assuming that some unaccounted for phenomenon is responsible for deviations between observed and theoretical LFs. It also gives a great amount of confidence in stellar evolution models that use up-to-date physics, such as DSEP. Furthermore, the comparison between DSEP and VandenBerg et al. (2006) LFs and the successes and failures in matching the observed LFs of low-metallicity globular clusters supports the inclusion of gravitational settling and microscopic diffusion in stellar evolution models, and the implied reduction in globular cluster ages of order 1 Gyr.

7.3. *The RGB Bump*

The bump is caused by an increase in the hydrogen content of the material fed into the hydrogen-burning shell in stars along the RGB. This increase comes when the shell passes through the former base of the convection zone (Iben 1968). While it is difficult to make a concrete comparison due to the large error bars in the LF along the RGB, after examining the best matches it appears that M92's bump is approximately 0.4 mag fainter than the theoretical bump. This agrees with previous results from Fusi Pecci et al. (1990), which found a 0.4 mag difference for a sample of 13 clusters. Two possible explanations for the difference exist: either the hydrogen-burning shell has moved more rapidly than expected, or convection has penetrated farther into the star than expected, perhaps through a mechanism such as convective overshoot. In addition, recent results (Bjork & Chaboyer 2006) suggest that the location of the bump is extremely dependent on metallicity and composition, with 0.2 mag or more changes being possible within reasonable ranges of metallicity and α-enhancement.

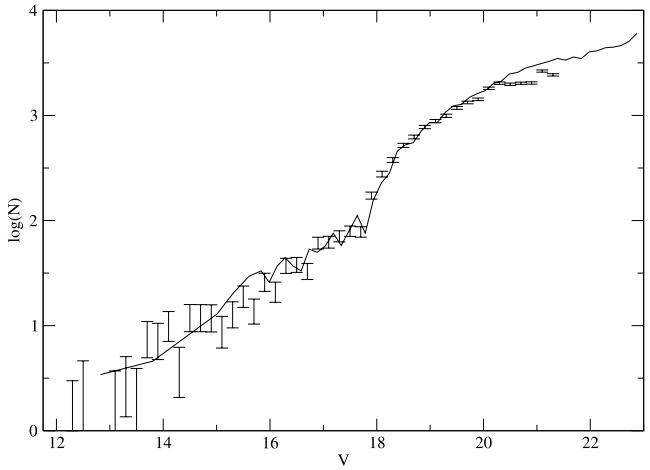

FIG. 11.—Sandquist et al. (1999) M30 LF and our LF with 1 σ error bars in the V band. For clarity, the error bars have been omitted from the M30 LF.

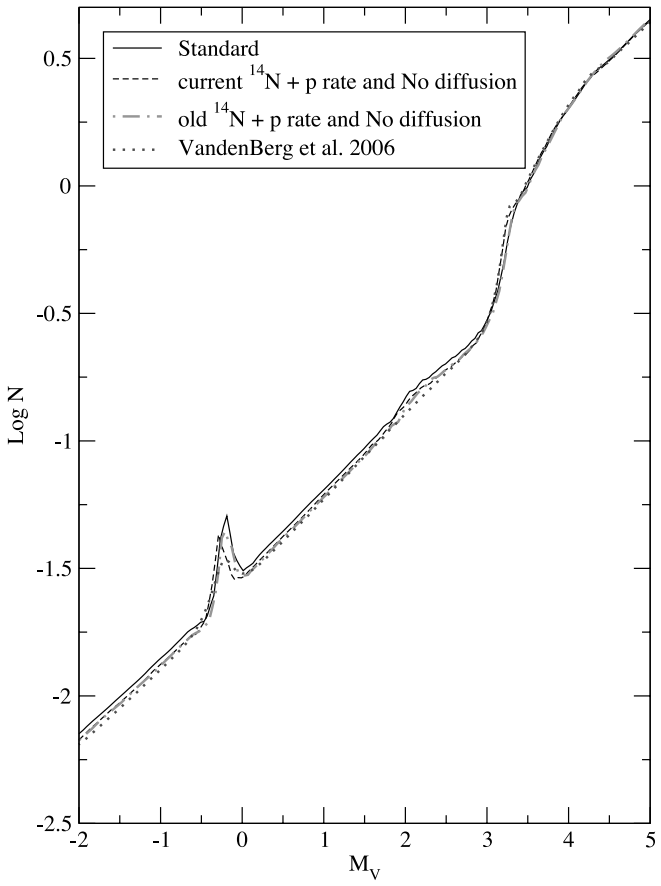

FIG. 12.—The 14 Gyr DSEP LFs with and without current reaction rates and diffusion compared to VandenBerg et al. (2006) LFs. When normalized to the MS, the VandenBerg et al. (2006) models have 9% fewer stars along the RGB. This decrease results in the excess of stars found in Sandquist et al. (1999). [*See the electronic edition of the Journal for a color version of this figure.*]

8. CONCLUSIONS

1. This paper finds good agreement between theoretical LFs and observations in terms of relative star counts along the MS, SGB, and RGB in the M92 LF. While the LFs are noisy in the RGB region, the theoretical LF matches the observed LF within the error bars. The result is further strengthened by the use of two independent data sets: the ground-based observations and the *HST* observations.

2. Contrary to previously published results, we find no subgiant excess in comparisons of the M92 LF to DSEP LFs, the M92 LF to the Sandquist et al. (1999) LF of M30, or the M30 LF directly to the DSEP LFs. It appears that the subgiant excess found

in previous works is due to an erroneous underprediction of the models rather than a real excess of stars in the cluster. Direct comparison of DSEP LFs to VandenBerg et al. (2006) LFs reveals that gravitational settling and microscopic diffusion all combine to better fit observations. Thus, observations of metal-poor globular clusters support the inclusion of these effects in stellar evolution models and their implied reduction in globular cluster ages.

3. Using two separate methods to compare the theoretical and observed LFs, it is possible to constrain the age of the cluster to 14.2 ± 1.2 Gyr, with an absolute distance modulus of 14.60 ± 0.09. In all cases, the comparison models included diffusion.

4. While the age determined for M92 appears to be too large, within the error bars it is consistent with the recent *Wilkinson Microwave Anisotropy Probe* results of the age of the universe of 13.7 ± 0.2 Gyr (Spergel et al. 2003). Accounting for the error bars, it is also consistent within 1 σ with the mean age of the oldest globular clusters: 12.6 ± 1.2 Gyr, based on the luminosity of the turnoff in Krauss & Chaboyer (2003).

Based on the observations made with the NASA/ESA *Hubble Space Telescope*, obtained from the Data Archive at the Space Telescope Science Institute, which is operated by the Association of Universities for Research in Astronomy, Inc., under NASA contract NAS5-26555. These observations are associated with program GO-9453.

REFERENCES

Bevington, P. R., & Robinson, D. K. 1992, Data Reduction and Error Analysis for the Physical Sciences (New York: McGraw-Hill)
Bjork, S. R., & Chaboyer, B. 2006, ApJ, 641, 1102
Bolte, M. 1994, ApJ, 431, 223
Brown, T. M., et al. 2005, AJ, 130, 1693
Chaboyer, B., Fenton, W. H., Nelan, J. E., Patnaude, D. J., & Simon, F. E. 2001, ApJ, 562, 521
Chaboyer, B., Sarajedini, A., & Demarque, P. 1992, ApJ, 394, 515
Chieffi, A., Straniero, O., & Salaris, M. 1991, in ASP Conf. Ser. 13, The Formation and Evolution of Star Clusters, ed. K. Janes (San Francisco: ASP), 219
Dean, J. F., Warren, P. R., & Cousins, A. W. J. 1978, MNRAS, 183, 569
Faulkner, J., & Swenson, F. J. 1993, ApJ, 411, 200
Formicola, A., et al. 2004, Phys. Lett. B, 591, 61
Fusi Pecci, F., Ferraro, F. R., Crocker, D. A., Rood, R. T., & Buonanno, R. 1990, A&A, 238, 95
Gallart, C., Zoccali, M., & Aparicio, A. 2005, ARA&A, 43, 387
Harris, W. E. 1996, AJ, 112, 1487
Kraft, R. P., & Ivans, I. I. 2003, PASP, 115, 143
Krauss, L. M., & Chaboyer, B. 2003, Science, 299, 65
Lee, K. H., Lee, H. M., Fahlman, G. G., & Lee, M. G. 2003, AJ, 126, 815
Iben, I. 1968, Nature, 220, 143
Piotto, G., Cool, A. M., & King, I. R. 1997, AJ, 113, 1345
Renzini, A., & Fusi Pecci, F. 1988, ARA&A, 26, 199
Robin, A. C., Reylé, S., Derriére, S., & Picaud, S. 2003, A&A, 409, 523
Rood, R. T., et al. 1999, ApJ, 523, 752
Sandquist, E. L., Bolte, M., Langer, G. E., Hesser, J. E., & de Oliveira, C. M. 1999, ApJ, 518, 262
Sandquist, E. L., Bolte, M., Stetson, P. B., & Hesser, J. E. 1996, ApJ, 470, 910
Sirianni, M., et al. 2005, PASP, 117, 1049
Spergel, D. N., et al. 2003, ApJS, 148, 175
Stetson, P. B. 1987, PASP, 99, 191
———. 1994, PASP, 106, 250
———. 2000, CADC Astronomical Standards (Ottawa: CADC), http://cadcwww.dao.nrc.ca/standards/
VandenBerg, D. A., Bergbusch, P. A., & Dowler, P. D. 2006, ApJS, 162, 375
VandenBerg, D. A., & Clem, J. L. 2003, AJ, 126, 778
Zinn, R., & West, M. J. 1984, ApJS, 55, 45